V European Conference on Computational Fluid Dynamics
ECCOMAS CFD 2010
J. C. F. Pereira and A. Sequeira (Eds)
Lisbon, Portugal,14-17 June 2010

TIME STEPPING AND LINEAR STABILITY OF RUNGE-KUTTA DISCONTINUOUS GALERKIN METHODS ON TRIANGULAR GRIDS

Thomas Toulorge* **and Wim Desmet†**

*K.U. Leuven, Dept. of Mechanical Engineering
Celestijnenlaan 300, B-3001 Heverlee, Belgium
e-mail: thomas.toulorge@mech.kuleuven.be
†K.U. Leuven, Dept. of Mechanical Engineering
Celestijnenlaan 300, B-3001 Heverlee, Belgium
e-mail: wim.desmet@mech.kuleuven.be

Key words: Discontinuous Galerkin Method, Runge-Kutta, Stability Analysis

Abstract. *The influence of element shape on the stability of a Runge-Kutta Discontinuous Galerkin method is systematically investigated, in order to improve the time step calculation in practical simulation. The maximum time step for stability is determined by comparing the eigenvalue spectrum of the semi-discrete scalar advection operator to the stability region of the Runge-Kutta integrator. Stability analyses are performed with a broad range of structured periodic triangular grids, all elements of each grid having the same shape, so that each element shape can be associated to a stability bound. Maximum Courant numbers are computed for Carpenter's low-storage (4,5) Runge-Kutta scheme, based on three different measures of the element size. Lower values of the maximum Courant number, to be used in practical simulations, are provided, and the accuracy of the CFL condition is assessed for each element size measure. In order to remedy the relative lack of reliability of CFL conditions, a simplified procedure for stability analysis is presented, that can be used for maximum time step calculation in practical simulations. It is shown in two examples involving respectively an unstructured and a hybrid grid, that it compares favorably to the CFL conditions.*

1 INTRODUCTION

Among the numerous numerical methods used to solve hyperbolic partial differential equations on unstructured grids, the Discontinuous Galerkin (DG) Method is receiving growing attention in different fields like Computational ElectroMagnetics, Computational Fluid Dynamics (CFD) or Computational AeroAcoustics (CAA). Its ability to obtain solutions with arbitrarily high order of accuracy is a particularly interesting feature. Other advantages over concurrent high-order methods like Finite Differences are the straightforward formulation of boundary conditions, as well as the compactness of the scheme, that allows an efficient parallel implementation.

When solving time-dependent Partial Differential Equations (PDE's), the DG method is often combined with Runge-Kutta (RK) time integrators. In this case, there exists a maximum time step above which the scheme becomes unstable. A stability bound can be obtained by applying to each element in the computational domain the well-known Courant-Friedrichs-Levy (CFL) inequality:

$$\|\mathbf{a}\| \frac{\Delta t}{h} \leq C \tag{1}$$

where $\|\mathbf{a}\|$ is the magnitude of the largest characteristic quantity of the hyperbolic system, Δt is the time step, h is a measure of the element size and C is a constant that depends on the spatial and time discretization methods. The left-hand side of inequality (1) is called the Courant number.

With one spatial dimension, this condition has been thoroughly studied and found to provide a satisfying bound for the maximum time step,[1] as the element size is well-defined in a 1D space. However, it is not well adapted to 2D and 3D, because the element shape is then only taken into account in the parameter h. In Ref. 2, the stability of the DG method combined with Strong-Stability-Preserving RK schemes is studied for low orders of the DG polynomial basis. However, that work is restricted to only two structured triangular grid configurations, and does not deal with the influence of element shape on the stability bounds. Yet, evaluating the dependency of the maximum Courant number on geometrical characteristics of the element, and determining the size measure h that minimizes this dependency, would improve the calculation of the time step to be specified in practical simulations. The work presented in this paper aims at evaluating the impact of the shape of 2D triangular elements on the CFL condition, and providing satisfying stability bounds for the Courant number, which could be used as simulation guidelines. A simplified stability analysis method, meant to be a more reliable alternative to the CFL condition for time step calculation in practical simulations, is also described.

In Sec. 2, a method to analyze the stability of RK-DG methods for triangular elements with various shapes is described. Results on the accuracy of the CFL condition, as well as practical values for the maximum Courant number, are presented in Sec. 3. The development of an advanced procedure for time step calculation, based on a simplified stability analysis, is explained in Sec. 4. Examples of time step calculations on two grids

are given in Sec. 5. Finally, conclusions are drawn in Sec. 6.

2 METHOD

2.1 Discontinuous Galerkin Method

As a model for hyperbolic conservation laws, the scalar advection equation over a domain with periodic boundary conditions is considered:

$$\frac{\partial q}{\partial t} + \frac{\partial a_r q}{\partial x_r} = 0 \tag{2}$$

where q is the unknown, t is the time, x_r is the r-th space coordinate, and a_r is the r-th component of the constant advection vector $\mathbf{a}$. Einstein's summation convention is used over the r index.

For each element Ω resulting from the partitioning of the computational domain, a basis $\mathcal{B} = \{\varphi_j,\, j = 1 \dots N_p\}$ is defined, in which the components φ_j are polynomials of order p supported in Ω, with $N_p = \frac{(p+1)(p+2)}{2}$ for triangular elements. An approximation q^Ω of q on Ω is obtained by a projection on this basis:

$$q^\Omega = \sum_{j=1}^{N_p} q_j^\Omega \varphi_j$$

Applying the Discontinuous Galerkin procedure to Eq. (2) results in:

$$\mathbf{M}^\Omega \frac{\partial q^\Omega}{\partial t} - \mathbf{K}_\mathbf{r}^\Omega a_r q^\Omega + \sum_{i=1}^{3} \mathbf{M}^{\partial\Omega_i} F^{\partial\Omega_i} = 0 \tag{3}$$

with:

$$\begin{aligned}
\mathbf{M}_{kj}^\Omega &= \int_\Delta \varphi_k \varphi_j \left|J^\Omega\right| d\Delta \\
\left(\mathbf{K}_\mathbf{r}^\Omega\right)_{kj} &= \int_\Delta \left(J^\Omega\right)_{sr}^{-1} \frac{\partial \varphi_k}{\partial \xi_s} \varphi_j \left|J^\Omega\right| d\Delta \\
\mathbf{M}_{kj}^{\partial\Omega_i} &= \int_{\partial\Delta_i} \varphi_k \varphi_j \left|J^{\partial\Omega_i}\right| d\partial\Delta_i
\end{aligned} \tag{4}$$

where each element Ω is mapped onto a unique reference element Δ by a function with Jacobian matrix J^Ω. Likewise, each element edge $\partial\Omega_i$ is mapped onto a unique edge $\partial\Delta_i$ of Δ by a function with Jacobian matrix $J^{\partial\Omega_i}$. The basis $\mathcal{B}$ is then expressed in Δ with reference coordinates (ξ_1, ξ_2). In Eq. (3), $F^{\partial\Omega_i}$ is an approximation of the numerical flux computed on the element edge $\partial\Omega_i$ that is common to Ω and its neighbour Ω_i'. In this work, $F^{\partial\Omega_i}$ is either the Lax-Friedrichs flux:

$$F^{\partial\Omega_i} = \frac{1}{2}\left[(\mathbf{a}\cdot\mathbf{n})\left(q^\Omega + q^{\Omega'}\right) - \|\mathbf{a}\|\left(q^{\Omega'} - q^\Omega\right)\right] \tag{5}$$

or the upwind flux:

$$F^{\partial\Omega_i} = \begin{cases} (\mathbf{a}\cdot\mathbf{n})\, q^{\Omega}, & \mathbf{a}\cdot\mathbf{n} \geq 0 \\ (\mathbf{a}\cdot\mathbf{n})\, q^{\Omega'}, & \mathbf{a}\cdot\mathbf{n} < 0 \end{cases} \tag{6}$$

$\mathbf{n}$ being the outgoing unit normal to the element edge $\partial\Omega_i$. These two choices of flux are the most widely used to solve linear PDE's.

2.2 Stability Analysis

2.2.1 Semi-Discrete Discontinuous Galerkin Operator

The global DG space operator $\mathbf{L}$ can be assembled directly by applying Eq. (3) for all elements of a grid, yielding:

$$\frac{\partial \tilde{q}}{\partial t} \;=\; \mathbf{L}\,\tilde{q}$$

where $\tilde{q}$ contains the semi-discrete solution for all degrees of freedom in the computational domain.

In this work, stability analyses are performed with structured grids made up of periodic patterns of congruent elements, as illustrated in Fig. 1. In this case, a Von Neumann-like procedure is used as an alternative to the global operator assembly. It consists in considering harmonic solutions on a single pattern:

$$q \;=\; \hat{q}\, e^{i(k_x \Delta x + k_y \Delta y)}$$

and exploiting the periodicity of patterns to formulate the semi-discrete operator:

$$\frac{\partial \hat{q}}{\partial t} \;=\; \mathbf{L}\left(k_x, k_y\right)\, \hat{q}$$

where $\hat{q}$ represents the complex amplitude of the solution for all degress of freedom in a pattern.

2.2.2 Stability of Runge-Kutta Methods

The stability of a RK method is determined by its characteristic polynomial P obtained by applying the time integration scheme to the model equation:

$$\frac{\partial u}{\partial t} \;=\; \lambda u$$

with $\lambda \in \mathbb{C}$. The time stepping scheme can then be formulated as $u^{n+1} = P\left(z\right) u^n$, where $z = \lambda \cdot \Delta t$, and the absolute stability region S of the RK scheme is given by:

$$S \;=\; \{z : |P\left(z\right)| \leq 1\}$$

2.2.3 Stability of the Fully Discrete Scheme

To evaluate the stability of the fully discrete RK-DG method with a given time step Δt, the eigenvalues $\lambda(\mathbf{L})$ of the semi-discrete operator $\mathbf{L}$ are computed, and the spectrum $\lambda \cdot \Delta t$ is compared to S, as illustrated in Fig. 2. Although the presence of the whole spectrum inside S is not a sufficient condition for the stability of the fully discrete scheme, it provides an excellent guideline for the choice of Δt.[3] In order to find the maximum allowable time step Δt_{max} for stability, a simple bisection method is applied to $P(\lambda \cdot \Delta t)$. The maximum Courant number ν is then computed as

$$\nu(\mathbf{a}) = \|\mathbf{a}\| \frac{\Delta t_{max}}{h}$$

for a given measure h of the element size.

2.3 Database

To determine the dependance of the stability bound on the triangle shape, stability analyses are performed on various grids made up of periodic patterns (see Fig. 1), in which all elements are congruent. The triangle shape, common to all elements in a grid, can be uniquely determined by three quantities (e.g. three side lengths). However, it can be deduced from Eqs. (3) and (4) that the semi-discrete operator $\mathbf{L}$ is inversely proportional to a scale size, so that only two independant parameters need to be studied. Thus, the horizontal edge length Δx is fixed, and the vertical element height Δy and mesh inclination α (see Fig. 1) are varied to obtain 42 different patterns (thus 42 different grids). Fig. 3 shows the shape of the 42 different elements. The grids are characterized by the triangle aspect ratio γ, which is commonly considered as a grid quality measure in meshing methods:

$$\gamma = 2\frac{r_{inner}}{r_{circum}}$$

where r_{inner} is the radius of the inscribed circle and r_{circum} is the radius of the circumcircle of the triangle. The grid quality measure γ varies from 0.00176 to 0.988 with a mean of 0.304. Its distribution is shown in Fig. 4.

It can be seen from Eqs. (3), (5) and (6) that $\mathbf{L}$ is proportional to the advection velocity $\|\mathbf{a}\|$, so that one can set $\|\mathbf{a}\| = 1$, and study only the effect of the advection direction θ with $\mathbf{a} = (\cos\theta, \sin\theta)$. θ varies in the range $[-180°, 180°]$ with a step of 4° and a stability analysis is carried out for each value of $\mathbf{a}$.

3 CFL CONDITION

The results are obtained with Carpenter's low-storage (4,5) RK scheme,[4] that is particularly appropriate for aeroacoustic propagation and other wave propagation problems. The same method can be applied to any RK scheme.

The maximum Courant number $\nu(\mathbf{a})$ is then calculated for three different element size measures h: the shortest edge in the triangle (ν^l), the shortest height in the triangle (ν^h),

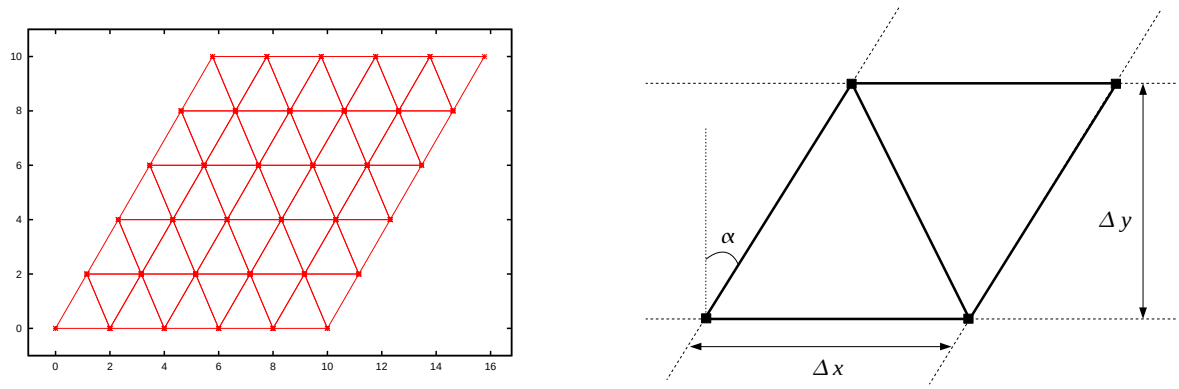

(a) (b)

Figure 1: Structured grid (a) and sketch of the periodic pattern of elements (b) used for stability analysis.

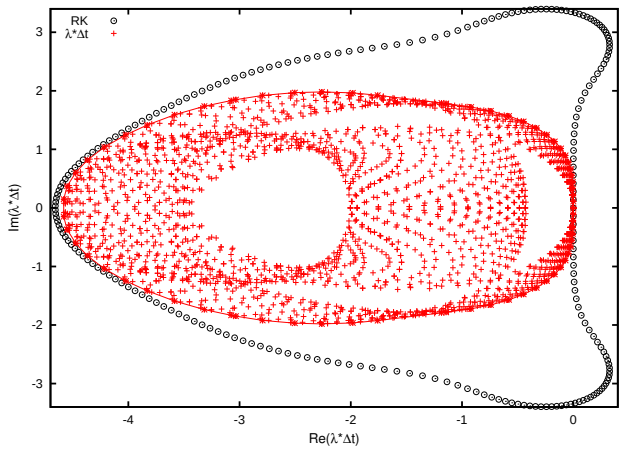

Figure 2: Stability plot for the 2D DG space operator ($p = 1$).

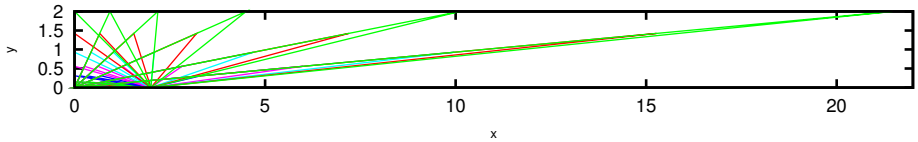

Figure 3: Lower-left element of all patterns used for the stability analysis.

and the radius of the inscribed circle (ν^r). Only the minimum value $\nu_{min} = \min_\theta \nu(\theta)$ is retained for each grid, since the characteristic directions cannot be determined *a priori* for most hyperbolic equations of practical interest.

3.1 Results for the Lax-Friedrichs Flux

Fig. 5 shows the three types of maximum Courant number in function of grid quality obtained with the Lax-Friedrichs flux at order $p = 5$. It can be noted that ν^l exhibits a large dispersion, especially for low mesh quality. This is due to the fact that low values of Δt_{max} are obtained with triangles that have one short edge, but also with "flat" triangles that have three long edges (i.e. triangles with two small and one large angle). The maximum Courant number ν^l based on the shortest edge is therefore not appropriate for triangular grids, and should be considered as unreliable for time step calculation in practical simulations. This is confirmed by Table 1, which contains the maximum deviation from the minimum value:

$$D = \frac{\max(\nu_{min}) - \min(\nu_{min})}{\min(\nu_{min})}$$

for ν^l_{min}, ν^h_{min} and ν^r_{min} with order p up to 10, obtained with the Lax-Friedrichs flux. These data suggest that ν^r_{min} is a better measure at low order p, whereas ν^h_{min} is better at higher order p. Minimum values of ν^l_{min}, ν^h_{min} and ν^r_{min}, that guarantee stability with any element shape, are provided for order p up to 10 in Table 2.

p	1	2	3	4	5	6	7	8	9	10
ν^l_{min}	948	942	936	946	951	944	944	944	943	944
ν^h_{min}	26	31	28	26	22	22	19	19	17	17
ν^r_{min}	23	20	21	19	23	24	27	27	30	29

Table 1: Maximum deviation D from the minimum value for maximum Courant numbers ν^l_{min}, ν^h_{min} and ν^r_{min} with order p from 1 to 10 with the Lax-Friedrichs flux, in percent.

3.2 Results for the Upwind Flux

Fig. 6 shows the three types of maximum Courant number in function of grid quality obtained with the upwind flux at order $p = 5$. Again, it is clear that the maximum Courant number ν^l based on the shortest edge is a bad choice, for the reasons explained in Sec. 3.1. Moreover, ν^r varies significantly, with low values for low quality elements and higher values for higher quality elements. ν^h, however, exhibits a remarkably low deviation. This is confirmed by Table 3, where the results for the maximum deviation from the minimum value show that the maximum Courant number ν^h based on the shortest height is the

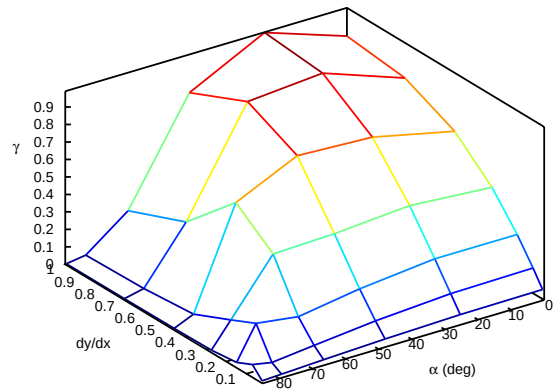

Figure 4: Mesh quality measure γ in function of the pattern aspect ratio $\Delta y/\Delta x$ and mesh inclination α.

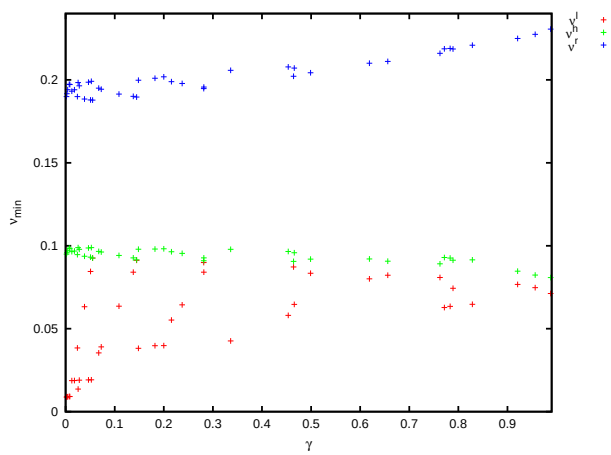

Figure 5: Maximum Courant numbers ν^l_{min}, ν^h_{min} and ν^r_{min} for the Lax-Friedrichs flux in function of grid quality measure γ at order $p = 5$.

p	1	2	3	4	5	6	7	8	9	10
ν^l_{min}	0.044	0.026	0.017	0.012	0.0088	0.0067	0.0053	0.0042	0.0035	0.0029
ν^h_{min}	0.402	0.226	0.154	0.106	0.0809	0.0612	0.0497	0.0398	0.0336	0.0280
ν^r_{min}	0.930	0.539	0.365	0.253	0.188	0.141	0.112	0.0896	0.0740	0.0618

Table 2: Minimum value of the maximum Courant numbers ν^l_{min}, ν^h_{min} and ν^r_{min} for order p from 1 to 10 with the Lax-Friedrichs flux.

only suitable choice, being particularly accurate at high order p. Minimum values of ν^l_{min}, ν^h_{min} and ν^r_{min} are given for order p up to 10 in Table 4.

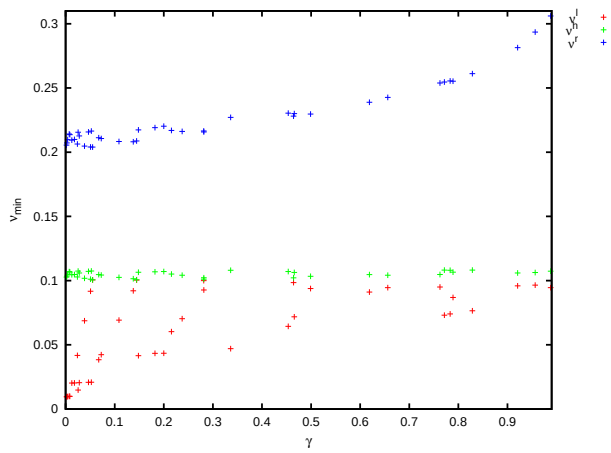

Figure 6: Maximum Courant numbers ν^l_{min}, ν^h_{min} and ν^r_{min} for the upwind flux in function of grid quality measure γ at order $p = 5$.

p	1	2	3	4	5	6	7	8	9	10
ν^l_{min}	954	945	939	946	955	948	956	971	959	950
ν^h_{min}	12	12	11	8.2	7.6	6.2	6.1	5.1	5.0	4.4
ν^r_{min}	53	57	54	52	50	49	49	46	48	47

Table 3: Maximum deviation D from the minimum value for maximum Courant numbers ν^l_{min}, ν^h_{min} and ν^r_{min} with order p from 1 to 10 with the upwind flux, in percent.

4 SIMPLIFIED STABILITY ANALYSIS PROCEDURE

The results reported in Sec. 3 show that the maximum Courant number can vary depending on the element shape. The amplitude of this variation, as well as the best element size measure to use, depend on the numerical flux type and the order p of the polynomial basis. Thus, using minimum values provided in Tables 2 and 4 in a real-world simulation may result in suboptimal time step, in spite of ensuring stability for any element shape.

On the other hand, one could think of calculating the time step by considering each element in the grid, and performing Von-Neumann analyses for the corresponding periodic

pattern with varying advection direction, as described in Sec. 2.2. Unfortunately, this procedure is far too expensive computationally.

However, some observations on the database of stability results described in Sec. 2.3 enable to considerably simplify the stability analysis process. These observations are related hereafter.

4.1 Estimation of Δt from the Spectral Radius

As seen in Fig. 2, the shapes of the RK stability region S and of the locus $z = \lambda \cdot \Delta t$ in the complex plane are not trivial, so that a non-linear search method has to be used to find the exact Δt_{max}. However, the eigenvalues of largest complex magnitude are usually among the first to leave the stability region (close to the real axis) when increasing Δt. A reasonable estimation of the time step can thus be obtained with:

$$\Delta t_{max} \approx \frac{\max |\Re(S)|}{\rho(\mathbf{L})} \tag{7}$$

where $\rho(\mathbf{L}) = \max \|\lambda\|$ is the spectral radius of the semi-discrete space operator $\mathbf{L}$. For Carpenter's low-storage (4,5) RK scheme, $\max |\Re(S)| = 4.656$.

Table 5 shows the maximum error in the estimated Δt_{max} over all element shapes and all advection directions mentioned in Sec. 2.3. For the Lax-Friedrichs flux, the error becomes negligible at order higher than $p = 3$, whereas the prediction is less accurate for the upwind flux.

4.2 Extrapolation from Order $p = 2$

A careful analysis of the stability database results shows that it is possible to devise approximate scaling laws for the spectral radius $\rho(\mathbf{L})$ in function of the order p. For reasons explained in Sec. 4.3, it is particularly interesting to relate $\rho(\mathbf{L})$ to the spectral radius $\rho(\mathbf{L}_{p=2})$ of the semi-discrete operator at order $p = 2$ for the same element shape and advection vector $\mathbf{a}$.

Fig. 7 shows the spectral radius $\rho(\mathbf{L})$ at order $p = 5$ in function of the spectral radius $\rho(\mathbf{L}_{p=2})$ at order $p = 2$, for the Lax-Friedrichs flux with advection $\mathbf{a} = (1, 0)$. The scaling

p	1	2	3	4	5	6	7	8	9	10
ν^l_{min}	0.044	0.026	0.017	0.013	0.0095	0.0075	0.0061	0.0051	0.0043	0.0037
ν^h_{min}	0.461	0.267	0.180	0.131	0.101	0.0790	0.0644	0.0534	0.0450	0.0384
ν^r_{min}	0.934	0.541	0.366	0.266	0.204	0.160	0.130	0.109	0.0912	0.0779

Table 4: Minimum value of the maximum Courant numbers ν^l_{min}, ν^h_{min} and ν^r_{min} for order p from 1 to 10 with the upwind flux.

of $\rho(\mathbf{L})$ when varying the element shape is well described by a linear law. However, this linear law depends on the advection direction θ, as made obvious in Fig. 8.

In the case of the upwind flux, a proportionality relation appears to be accurately satisfied, the proportionality constant being independent of the advection direction θ, as illustrated in Fig. 9.

Now, for reasons already mentioned in Sec. 2.3, $\rho(\mathbf{L})$ varies as the inverse of a scale size, and its scaling with respect to the order p is measured for elements with one edge fixed at length Δx. The scale factor can be taken into account for an arbitrary triangle by considering the length l of the edge corresponding to the horizontal edge of the database elements (with length Δx), and defining a *scaled* spectral radius:

$$\bar{\rho}\left(\mathbf{L}^{\Omega}\right) \;=\; \frac{l}{\Delta x}\,\rho\left(\mathbf{L}^{\Omega}\right)$$

In the general case, the scaling laws for the scaled spectral radius $\bar{\rho}\left(\mathbf{L}^{\mathbf{\Omega}}\right)$ be expressed as:

$$\bar{\rho}\left(\mathbf{L}^{\Omega}\right) \;=\; \alpha\,\bar{\rho}\left(\mathbf{L}^{\Omega}_{p=2}\right) \;+\; \beta$$

where α and β depend on θ for the Lax-Friedrichs flux, and α is independent of θ with $\beta = 0$ for the upwind flux. The spectral radius at any order p can then be computed with:

$$\rho\left(\mathbf{L}^{\Omega}\right) \;=\; \alpha\,\rho\left(\mathbf{L}^{\Omega}_{p=2}\right) \;+\; \beta\frac{\Delta x}{l} \tag{8}$$

provided that the values of α and β are tabulated for each value of p and, if applicable, for each value of θ.

4.3 Spectral Radius at Order $p = 2$

The spectral radius of the operator at order $p = 2$ can be computed by means of the Von-Neumann-like procedure described in Sec. 2.2. This process is still computationally intensive, as a whole range of modes (k_x, k_y) has to be considered: the semi-discrete space operator $\mathbf{L}(k_x, k_y)$ must be built and its eigenvalues computed for each value of (k_x, k_y).

However, the database results show that for even values of the order p, the maximum eigenvalue (and thus the spectral radius) is obtained for $(k_x, k_y) = (0, 0)$:

$$\rho\left(\mathbf{L}^{\Omega}_{p=2}\right) \;=\; \rho\left[\mathbf{L}^{\Omega}_{p=2}\left(k_x = 0, k_y = 0\right)\right]$$

p	1	2	3	4	5	6	7	8	9	10
Lax-Friedrichs Flux	16	7.4	2.3	0.1	0.1	0.1	0.1	0.1	0.1	0.1
Upwind Flux	16	15	14	11	11	10	10	9.2	9.7	8.9

Table 5: Error in the maximum time step Δt_{max} estimated from the spectral radius $\rho(\mathbf{L})$, in percent.

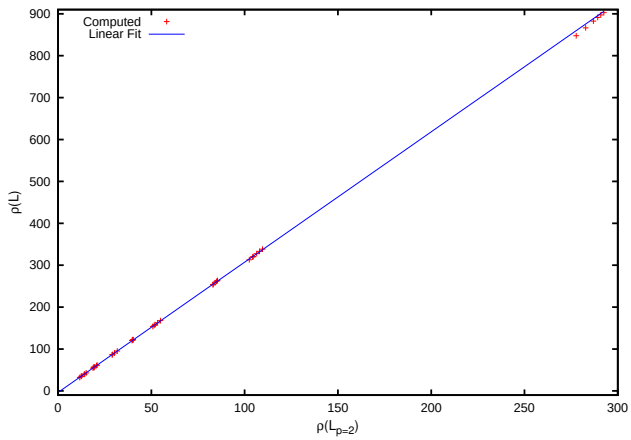

Figure 7: Spectral radius $\rho\left(\mathbf{L}^{\Omega}\right)$ at order $p=5$ in function of the spectral radius $\rho\left(\mathbf{L}^{\Omega}_{p=2}\right)$ at order $p=2$, for the Lax-Friedrichs flux, with horizontal advection direction.

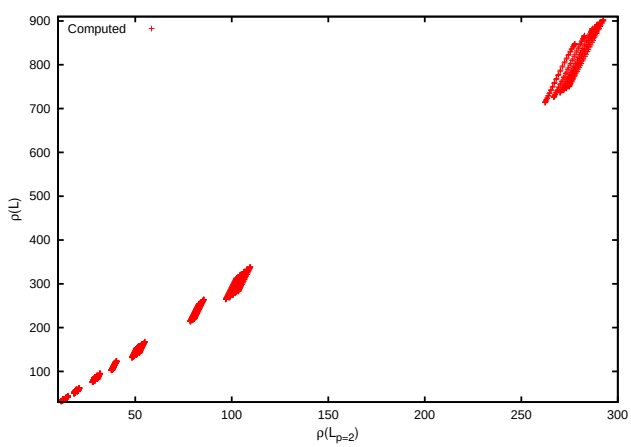

Figure 8: Spectral radius $\rho\left(\mathbf{L}^{\Omega}\right)$ at order $p=5$ in function of the spectral radius $\rho\left(\mathbf{L}^{\Omega}_{p=2}\right)$ at order $p=2$, for the Lax-Friedrichs flux, with all values of the advection direction θ.

This assumption is verified for all element shapes and all advection directions in the database, at order $p \in \{2, 4, 6, 8, 10\}$.

This reduces the computational effort for one element and one advection direction to one eigenvalue problem on the operator $\mathbf{L}_{p=2}\left(k_x = 0, k_y = 0\right)$ (i.e. a 12×12 matrix), which is affordable. The spectral radius can then be extrapolated to any order p, as explained in Sec. 4.2. The analytical expression of $\mathbf{L}_{p=2}\left(k_x = 0, k_y = 0\right)$ in function of the coordinates of the triangle vertices can be obtained by means of a Computer Algebra System and easily plugged in any Discontinuous Galerkin solver.

4.4 Full Procedure

To summarize, the full procedure to calculate the maximum time step for an arbitrary triangular grid is described by the following pseudo-code:

for each element Ω in the grid **do**
  for each value of θ **do**
    Compute $\rho\left(\mathbf{L}_{p=2}^{\Omega}\right)$ for $(k_x, k_y) = (0, 0)$
    Compute $\rho\left(\mathbf{L}^{\Omega}\right)$ from $\rho\left(\mathbf{L}_{p=2}^{\Omega}\right)$ with Formula (8).
    Compute Δt_{max} from $\rho\left(\mathbf{L}^{\Omega}\right)$ with Formula (7)
  end for
  Retain $\min_{\theta}\left(\Delta t_{max}\right)$
end for
Retain $\min_{\Omega}\left(\Delta t_{max}\right)$

This procedure can even be safely optimized by pre-selecting the elements Ω to be analyzed with a geometric criterion based on the CFL condition, instead of applying it to every element in the computational domain.

5 EXAMPLES

In order to illustrate the relative performance of the different methods, the maximum time step Δt_{max} allowed for stability is computed on two different triangular grids, on which periodic boundary conditions are imposed. The exact Δt_{max}, obtained by directly assembling the semi-discrete operator $\mathbf{L}$ for the whole grid, is compared to the CFL conditions based on the inner radius R_{inner} and on the shortest height H_{min}, as well as with the simplified stability analysis procedure. Given that the advection velocity is constant over the computational domain, the Δt_{max} computed by the CFL conditions is obtained for the smallest element in the grid.

The first grid, shown in Fig. 10, is unstructured and contains 334 triangular elements. The results of time step calculations at order $p = 4$ are given in Table 6. For both types of fluxes, the CFL condition based on the inner radius provides the smallest time step, whereas the simplified stability analysis method gives significantly better results.

The second grid, shown in Fig. 11, is composed of a structured part and an unstructured part, like those commonly used to resolve boundary layers in CFD or CAA applications. It contains 164 triangular elements. The results of time step calculations at order $p = 6$ are given in Table 7. Here again, the simplified stability analysis procedure performs best, whereas the CFL conditions give inferior results.

In these two examples, the performance of CFL conditions vary, depending on the type of flux and the type of grid. On the contrary, the simplified stability analysis method gives the best results in almost all conditions. One can note that the time step provided by the three methods can be far from optimal (less than half of the optimal time step with the hybrid grid and the upwind flux). This highlights the fact that local methods, based on applying criteria element by element, can only provide *bounds* for stability, and the global stability condition may be less restrictive. Nevertheless, a gain in time step similar to the one reached by the simplified stability analysis method over the CFL conditions in these examples, can lead to a significant reduction in CPU time for practical simulations.

Fluxes	Lax-Friedrichs	Upwind
Exact	0.0679	0.103
CFL – R_{inner} (% Error)	0.0463 (31.8%)	0.0486 (52.7%)
CFL – H_{min} (% Error)	0.0546 (19.7%)	0.0677 (34.1%)
Simplified Stability Analysis (% Error)	0.0545 (19.8%)	0.0789 (23.2%)

Table 6: Maximum time step computed exactly, with the CFL condition based on the inner radius and the shortest height, and with the simplified stability analysis procedure, for the unstructured grid of Fig. 10, at order $p = 4$.

Fluxes	Lax-Friedrichs	Upwind
Exact	$8.62{\cdot}10^{-4}$	$2.04{\cdot}10^{-3}$
CFL – R_{inner} (% Error)	$7.75{\cdot}10^{-4}$ (10.1%)	$8.80{\cdot}10^{-4}$ (56.9%)
CFL – H_{min} (% Error)	$6.94{\cdot}10^{-4}$ (19.5%)	$8.97{\cdot}10^{-4}$ (56.1%)
Simplified Stability Analysis (% Error)	$7.88{\cdot}10^{-4}$ (8.6%)	$9.87{\cdot}10^{-4}$ (51.7%)

Table 7: Maximum time step computed exactly, with the CFL condition based on the inner radius and the shortest height, and with the simplified stability analysis procedure, for the hybrid grid of Fig. 11, at order $p = 6$.

6 CONCLUSION

In this work, the stability of a RK-DG method has been systematically investigated for a set of structured triangular grids featuring a broad range of element shapes.

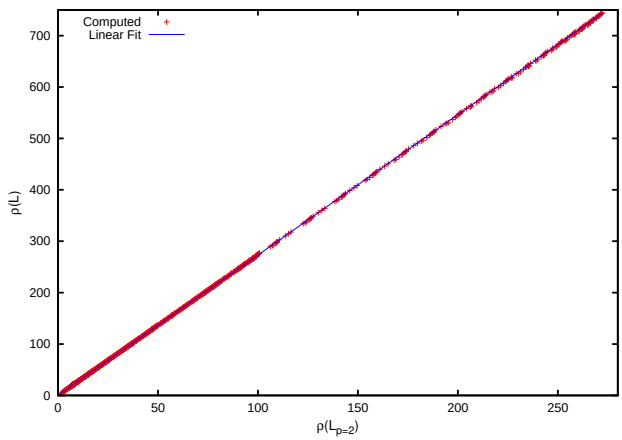

Figure 9: Spectral radius $\rho\left(\mathbf{L}^{\Omega}\right)$ at order $p = 5$ in function of the spectral radius $\rho\left(\mathbf{L}^{\Omega}_{p=2}\right)$ at order $p = 2$, for the upwind flux, with all values of the advection direction θ.

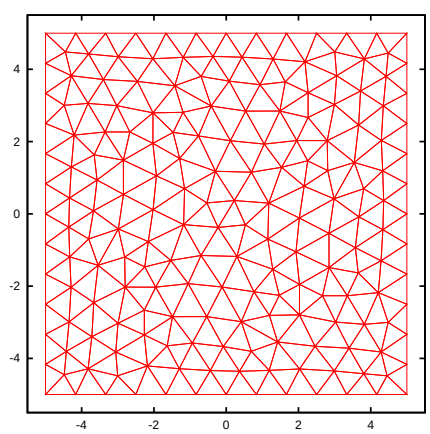

Figure 10: Unstructured grid used for validation.

Maximum Courant numbers have been computed for Carpenter's low-storage (4,5) RK scheme, based on three different measures of the element size. The results show that none of the three measures provide an unambiguous stability bound. The measure based on the shortest triangle edge is particularly unreliable, as it fails to detect ill-conditioned triangles with 3 long edges. The other two measures, based on the shortest triangle height and the radius of the inscribed circle, lead to maximum Courant numbers that can vary up to 30% in function of the element shape. Lower values of the maximum Courant number, to be used in practical simulations, are provided.

Based on a number of assumptions that are found to be valid (exactly or approximately) for the set of structured grids considered, it has been possible to reduce the stability analysis to a procedure that is computationally efficient enough to be used for time step calculation in practical simulations.

Two examples involving respectively an unstructured and a hybrid grid, showed that the CFL conditions perform irregularly, depending on the grid and the type of flux used. In all cases, the simplified stability analysis procedure gives an equal or better time step than the best CFL condition. However, the results obtained show the limitations of element-by-element criteria, as the stability bounds that they provide are significantly too restrictive compared to the global stability condition.

In the future, this work will be extended to 3D, in order to assess the accuracy of the CFL conditions and obtain practical values of the maximum Courant number for tetrahedral elements. Concerning the simplified stability analysis method, it will be checked whether the underlying assumptions also hold for elements with higher geometrical order. Indeed, CFL conditions cannot be applied to curved elements and there is currently no way to obtain stability bounds for the time step in this case.

ACKNOWLEDGEMENTS

The authors are grateful to Prof. Jean-François Remacle (Université Catholique de Louvain, Belgium) and to Prof. Johan Meyers (K.U. Leuven, Belgium) for valuable discussions about the stability of RK-DG methods. The useful suggestions of Drs. Wim De Roeck and Maarten Hornikx (K.U. Leuven, Belgium) are appreciated. Thomas Toulorge acknowledges the financial support of the European Commission through the Marie-Curie Reseach and Training Network "AETHER", Contract Nr. MRTN-CT-2006-035713.

REFERENCES

[1] B. Cockburn, C.W. Shu, *Runge–Kutta discontinuous Galerkin methods for convection dominated problems*, Journal of Scientific Computing, Vol. 16, pp. 173–261, 2001.

[2] E. Kubatko, C. Dawson, J.J. Westerink, *Time step restrictions for Runge–Kutta discontinuous Galerkin methods on triangular grids*, Journal of Computational Physics, Vol. 227, pp. 9697-9710, 2008.

[3] J.S. Hesthaven, T. Warburton, *Nodal Discontinuous Galerkin Methods: Algorithms, Analysis, and Applications*, Vol. 54, Springer Texts in Applied Mathematics, Springer Verlag, New York, p. 95, 2008.

[4] M.H. Carpenter, C.A. Kennedy, *A fourth-order 2N-storage Runge-Kutta scheme*, NASA TM 109112, 1994.

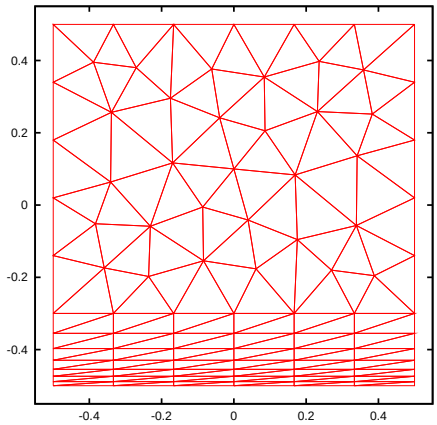

Figure 11: Hybrid grid used for validation.